Snapback - Novel Methods for the Analysis of Parted Mooring Lines and Resistance Structures

Author: Jordan A. Wolfe
Age (at Submission)**:** 34
Affiliations: Wolfe, Perth, Australia
Swinburne University of Technology, Melbourne, Australia
Contact: Jordan@wolfegroup.com.au

Declaration: The content presented in this paper is my own original works. Due acknowledgement is made to any other materials referenced in text.
The total word count of this paper, excluding figures, tables, and the table of references is 4,931 words.

Signed:

Keywords: Mooring Lines, Snapback, Dynamics, Resistance Structures, Structural Response.

Snapback is defined as the dynamic recoil of parted mooring lines accelerated under their own tension. In this paper, first-principles derivations of equations for snapback are presented using an extension to existing models for highly extensible cables (1). Validation is undertaken using non-linear transient dynamic finite element analysis (NLTD FEA), producing a database of 364,608 simulated events (~6×10^{12} datapoints). Snapback path envelopes are defined using novel meshing algorithms. NLTD FEA results are compared and demonstrate 96 - 99% accuracy against full-scale tests. Closed-form equations are presented, and their accuracy is compared to both the historical physical testing and computational results. The applicability of models for the dynamics of arresting structures for high-mass low-velocity collisions is explored briefly (2) and compared to explicit dynamic FEA models of arresting structures. Failure modes described by others (3, 4) are validated. The results provide a defensible basis for the estimation of snapback velocities and paths and enable Ultimate Limit State (ULS) design for snapback arresting structures. These works, in part, directly inform PIANC WG 251 and are intended to improve port safety worldwide.

1. INTRODUCTION

Snapback is a poorly quantified hazard in maritime operations, though it is catastrophic and often fatal. In Australia, snapback causes one fatality every five years (5), with one fatality every three years reported in other countries (6). When parted mooring lines strike personnel, 14% of events result in a fatality (7). Aside from these dangers, snapback is expensive. Lost time due to re-mooring and berth shutdowns for maintenance due to the risk snapback poses costs $250,000 per hour and billions annually in Australia, with similar values expected globally.

Australian ports have particularly high snapback risk due to large tidal ranges, large vessels, and exposed berths. Other ports around the world with similar challenges due to exposure have also recorded significant and fatal snapback events. As the effects of climate change increase wind speeds, currents, and tides, and as vessels continue to grow larger, the frequency and severity of snapback events are also expected to increase. That said, the current frequency of snapback events is poorly understood. Where data exists, it is expected to be underreported due to the complex operational structures of ports, jurisdictional constraints, and the sovereignty of foreign-flagged vessels who own the mooring lines. Recent estimates suggest that a snapback event occurs

somewhere in the world every 8 minutes, or 180 events every day (8). Despite the severity of these events, limited information exists in both historical and contemporary international design standards and guidelines. Whilst efforts have been made to quantify snapback velocity (9-12), very little research has been undertaken to quantify the expected path and spatial limits of snapback.

Consequently, many Australian ports have adopted barriers as the primary mitigation measure against snapback incidents. No design framework currently exists for assessing the performance of these barriers under high-velocity impact from recoiling lines and thus, in the absence of detailed guidance, design engineers generally adopt quasi-static force deflection models for approximating energy absorption. Recent physical testing has demonstrated that these theoretical models are incorrect and that failure occurs locally due to high-modal behaviour and localised stresses (4). This state of practice, wherein barriers are placed, without knowledge that they appropriately cover expected snapback paths, to arrest parted lines without suitable engineering design, creates a false sense of security whilst still potentially exposing people to harm.

2. HISTORICAL WORKS AND THE STATE OF CURRENT PRACTICE

Prior to World War 2, vessels were smaller and moored with manila, steel wire, and anchors. The advent of synthetic lines through the 1940's and 1950's, as well as wartime industrialisation led to an increase in snapback events. The United States Coast Guard (USCG) commenced research on snapback in 1966, undertaking full-scale physical testing (9). It was identified that lines could recoil in excess of 100 m/s with the capacity to destroy protective barriers. In Stuttgart in 1978, it was observed that the construction of lines affected their failure, leading to widespread adoption of 8-strand and higher braid which underwent so-called 'cascade failure', though velocities of up to 250 m/s were still recorded (10). The USCG undertook further studies, again noting velocities between 100 – 213 m/s, though they also noted energy losses between 8% and 42% for the parting of 8-strand lines (11). Larger energy losses, resulting in lower snapback velocities, were attributed to cascade failure. Recorded snapback velocities for various lines are given in Table 1, though tensions and energies are not normalised between the tests.

Table 1: Comparison of Snapback Velocities from Tests

Material and Construction	Parker (1966) Velocity (m/s)	Feyrer (1978) Velocity (m/s)	Bitting (1982) Velocity (m/s)
Nylon Double Braid	111 [A]	N/A	154
Nylon 8-Strand Plaited	97 [A,B]	200	161
Nylon 3-Strand Twisted	113 [A]	N/A	N/A
Nylon Cross Lay	N/A	N/A	114
Polyester Double Braid	118 [A]	N/A	110
Polyester 8-Strand Plaited	90 [A]	180	110
Polyester 3-Strand Twisted	90 [A]	N/A	N/A
Polypropylene 8-Strand Plaited	113 [A,B]	175	127
Polypropylene 3-Strand Twisted	86 [A]	N/A	44
Polypropylene 3-Strand Twisted (staple-fibre)	N/A	N/A	103
Kevlar	N/A	138	N/A
Nylon / Bridon	N/A	250	N/A
Kevlar / Bridon	N/A	233	N/A

Notes: A: Calculated from difference in kinetic energy and reported velocity value for polypropylene 7/8th inch in reference.
B: 8-Strand results taken from "plimoor" plait category which is a similar construction.

Despite the risk posed, very little has been done to provide models to quantify the energy and velocity of snapback events. Tjavaras (1) provides a foundation for the mechanics of highly

extensible cables, expanded upon in this paper, and computational analysis has been undertaken after significant snapback events (13, 14), but neither methodology is reflected in current or historical industry guidelines. What was shown historically was so-called 'Snap-Back Danger Zones', which first appeared in the Oil Company International Marine Forum's (OCIMF) Mooring Equipment Guidelines (MEG) 1st Edition in 1992 (15), reproduced below in Figure 1. These zones were defined as anywhere "within about a 10-degree cone around the line", which subsequent publications suggest was due to the sinusoidal buckling of the line (16).

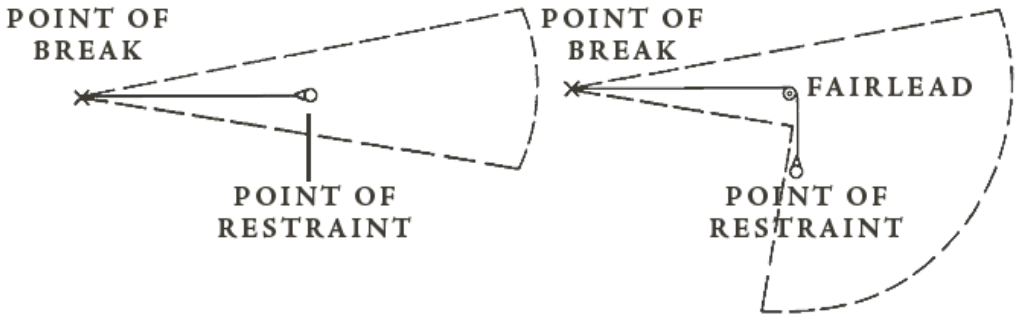

Figure 1: 'Snap-Back Danger Zones' as they appeared in OCIMF MEG1 (15), reproduced by the author.

On the 2nd of March 2015, the LNG carrier Zarga had a serious snapback event whereby a High Modulus Polyethylene (HMPE) line parted and struck an officer in the head (14). Computational analysis using explicit dynamic methods (14), the first of their kind, showed the path of the mooring line, which moved overboard before wrapping about the fairlead and whipping back to hit the office on the opposite side of fairlead. The insights generated by the investigation resulted in the retiring of snapback zones from OCIMF MEG4 in 2018, which instead states that "Although there are areas of increased snap-back risk, it is not possible to accurately calculate the whole range of snap-back danger zones needed to ensure personnel are safe" (6).

3. GAP IDENTIFICATION AND OBJECTIVES

The removal of snapback zones from industry guidelines renders decades of prior design and port operational practices obsolete (albeit, justifiably) and does so without offering a replacement framework. Further, it is noted that OCIMF MEG visualisations largely related to on-vessel snapback, and did not account for the motion of vessels, changes in tides, changes in mooring arrangements, and other such factors that make berth-side snapback zones significantly more dynamic. Even so, it remains the case that no guideline or standard ever published the design velocities observed in early physical testing, or any methodology that would allow for their application in the design of barriers.

Accordingly, the objective of this paper is to address this critical gap in maritime engineering by providing analytical, computational, and empirical methodologies for quantifying the dynamics, velocity, and path of snapback events. Whilst not fully resolved within this paper, the dynamics of arresting structures are explored and recent findings on the failure modes of existing structures subjected to snapback impacts are validated. The outcomes of this research will directly inform PIANC Working Group 251's (WG 251) report 'Guidance on the Design of Parted Mooring Line Arresting Systems', thereby allowing ports and engineers worldwide to adequately quantify snapback risk, and saving lives.

4. ANALYTICAL MODEL OF MOORING LINE SNAPBACK

Before defining the mathematical derivations of the dynamics of snapback, an illustrative example of mooring line failure is given to provide context.

4.1. Overview of Mooring Line Snapback

Mooring lines are ropes used to secure a vessel to a structure, as shown below in Figure 2. During this process, due to environmental loading or human operations, tension develops in the lines.

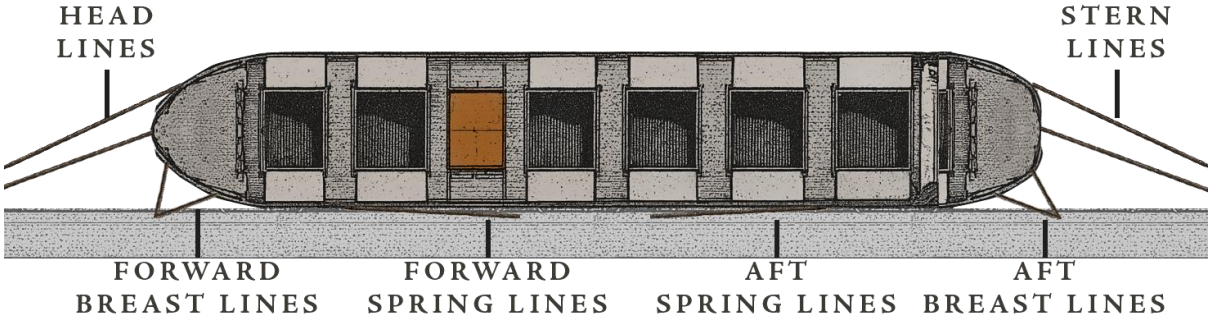

Figure 2: A typical mooring arrangement.

During mooring, wear occurs in the lines, typically at points of redirection, as shown below in Figure 3. This wear causes damage that reduces the mooring line's capacity.

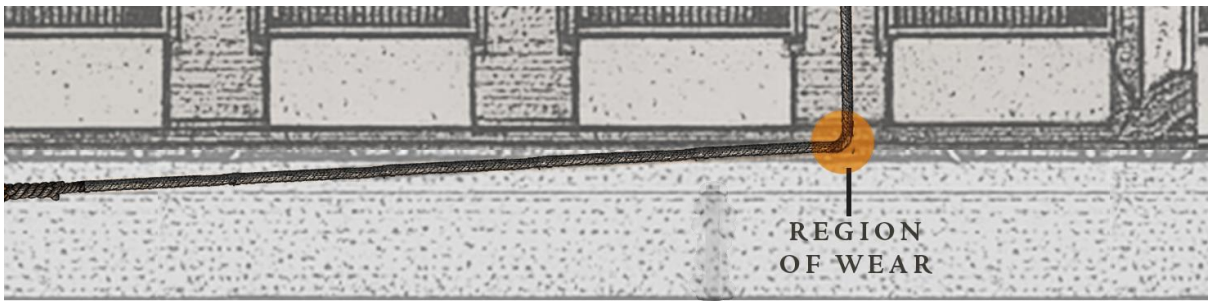

Figure 3: A region of wear induced by redirection about a fairlead.

Wear, combined with tension, can cause failure. Typically, failure occurs progressively as individual strands part before total failure, as shown in Figure 4. Whilst this usually occurs at the point of redirection, it can occur anywhere along the line due to historical damage as well.

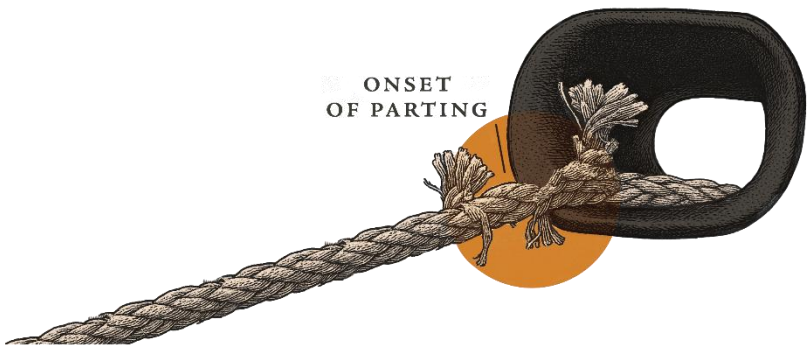

Figure 4: Cascade failure of a mooring line at the fairlead.

As the line parts, tension is released and propagates down the mooring line as a compressive wave at the speed of sound, or celerity, of the mooring line itself, which is a function of its material and geometry. This results in points along the mooring line still being in tension, whilst points closer to

the point of rupture begin to accelerate due to the asymmetry of forces. Due to the line construction, gravity, catenary, and any asymmetry in loading due to cascade failure, local buckling begins to develop along the length of the mooring line, as shown in Figure 5.

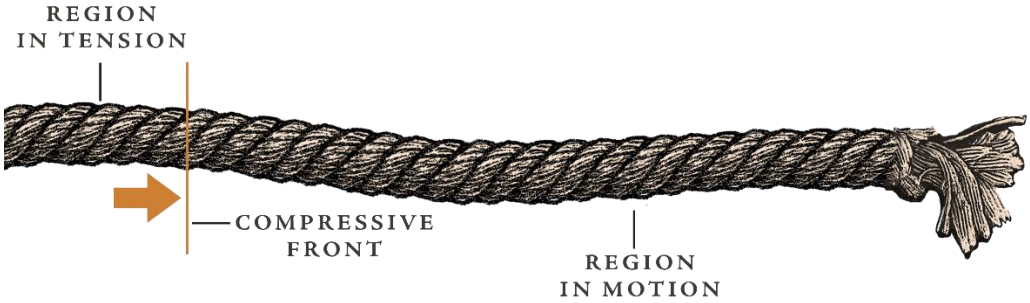

Figure 5: A compressive front propagating down the length of a parted mooring line.

Once the compressive front hits the restrained end, or any point of redirection, it partially reflects, inducing dynamic buckling as it and the line already in motion generate net compression along the mooring line, as shown in Figure 6.

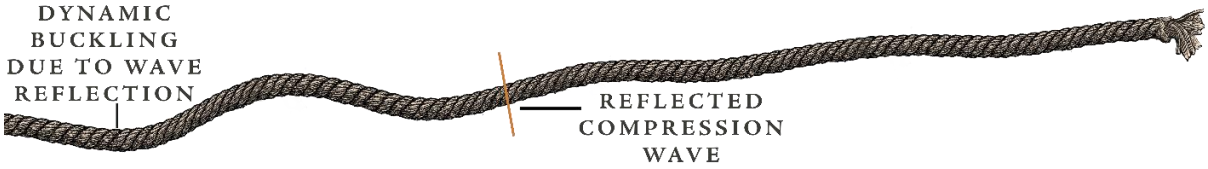

Figure 6: Dynamic buckling due to compressive wave reflection.

Where the line is straight between the rupture and restraint points, it follows a near-colinear path, though it may be redirected by physical interactions. In cases of curvature however, angular momentum is generated and the line follows a wider arc. Higher velocities may be observed in this case due to whipping, which causes momentum transfer and secondary acceleration of the free tip.

4.2. Mathematical Model of Snapback

This paper adopts the Tjavaras model (1) as its basis, proposing modifications thereafter to improve suitability for snapback analysis. The model derives the dynamics of the parted line from first principles of conservation and compatibility applied to a segment of homogeneous circular cross-section. Euler–Bernoulli buckling behaviour and a general single-valued tension–strain relation are used. A Lagrangian reference frame is adopted with unit vectors tangent, normal, and binormal to the mooring line itself. A rotational matrix using Euler parameters, to prevent singularities, maps the Lagrangian reference frame to the global Cartesian reference frame. The governing equations are written in vector form, as shown in Equation 1:

$$\frac{\partial \mathbf{Y}}{\partial s} + \mathbf{M}(\mathbf{Y})\frac{\partial \mathbf{Y}}{\partial t} + \mathbf{P}(\mathbf{Y}) = 0 \qquad \text{Eqn.1}$$

Where:

$$\mathbf{Y} = \left[\varepsilon \; S_n \; S_b \; u \; v \; w \; \beta_0 \; \beta_1 \; \beta_2 \; \beta_3 \; \Omega_1 \; \Omega_2 \; \Omega_3\right]^T \qquad \text{Eqn.2}$$

The matrix **M** and vector **P** are given in Appendix A. The modifications proposed later in this paper are already included.

The equations of motion are solved using a finite-difference box. Notably, Tjavaras adopts a variable breaking time function such that the speed of parting can be modelled:

$$P_h(t) = \begin{cases} P_h \cos^2\left(\frac{\pi}{2}\frac{t}{t_{br}}\right) & 0 \le t < t_{br} \\ 0 & t_{br} \le t \end{cases}, P_v(t) = \begin{cases} P_v \cos^2\left(\frac{\pi}{2}\frac{t}{t_{br}}\right) & 0 \le t < t_{br} \\ 0 & t_{br} \le t \end{cases} \quad \text{Eqn.3}$$

Where P_h and P_v describes the horizontal and vertical force arising from tension and catenary of the mooring line. A 50ms breaking case for a 60 m long line is reproduced from (1) in Figure 7, showing *s* (proximity to the retrained end where 60 m is the free tip) and velocity.

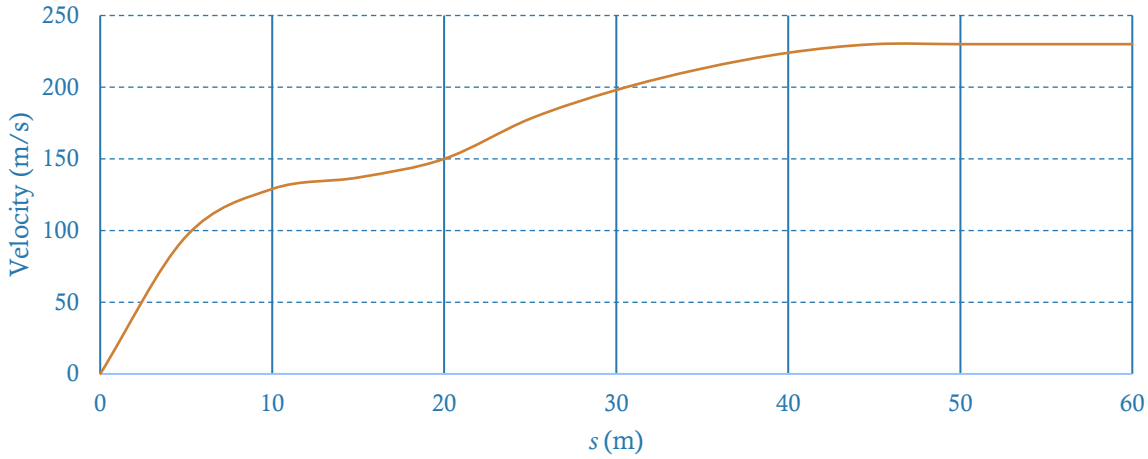

Figure 7: Velocity of a 60m line. Load: 450 kN, t_{br}: 50ms, t: 120 ms. Reproduced from Figure 7 of (1).

4.3. Computational Model of Snapback

A non-linear transient dynamic finite element analysis (NLTD FEA) is modelled to demonstrate agreement of such computational methods with the mathematical model shown in Section 4.2. A secant modulus of stiffness is adopted in lieu of the tension dependent model, and both strain and catenary are calculated in a non-linear static analysis first stage to provide the input conditions for the NLTD FEA. The adoption of a secant modulus produces a slightly greater overall stored energy and thus peak velocities between the models differ. The adopted parameters for the model are given below in Table 2, with outputs shown in Figure 8.

Table 2: Parameters for Computational Model of Snapback

Parameter	Computational Model	Tjavaras (as per (1))
E_s (GPa)	0.784	Non-uniform tension dependent
ν	0.499	0.5
ρ (kg/m^3)	1140	1140
D (mm)	50	50
Length (m)	60	60
Tension (kN)	450	450
t_{br}(ms)	50	50

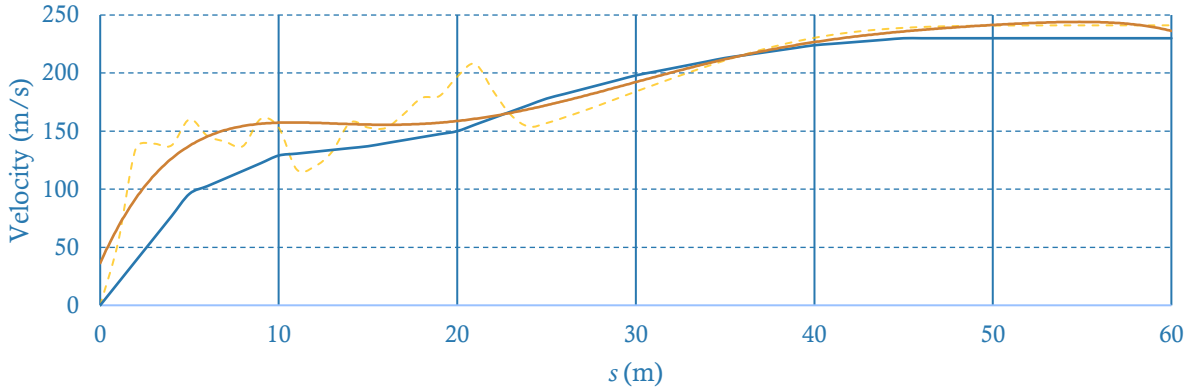

Figure 8: Velocity of a 60m line at t: 120 ms with parameters per Table 2. Computational model: yellow, Trendline of model: orange, Tjavaras model: blue.

4.4. Discussion on the Differences Between Models

Whilst the mathematical and NLTD FEA models show general agreement, differences are observed in the total energy in the system and the velocity close to s=0 m. Total energy differences are explained by the tension-strain relationship shown below in Equation 4:

$$T = p_1 \tanh(p_2\varepsilon + p_3) + p_4 + p_5\varepsilon \qquad \text{Eqn.4}$$

Where:

$$p_1 = 2.703 \times 10^5 N,\ p_2 = 10.2,\ p_3 = -2.128,\ p_4 = 2.627 \times 10^5 N,\ p_5 = 135.5\ N \qquad \text{Eqn.5}$$

Though Equations 4 and 5 better reflect real mooring lines, they introduce computational expense without significant improvement to results. The variability in the NLTD FEA velocities between s = 0 m and s = 25 m arises due to dynamic buckling, which is also present in the Tjavaras model, though the curve has been averaged as velocity may vary locally by ~±30% due to buckling.

4.5. Closed-form Approximation

Assuming total lossless energy transfer, a closed form approximation of velocity can be given by:

$$v(s) = 1.2\sqrt{\frac{2E_p}{m}}\tanh\left(\frac{4\pi\, s}{3L}\right) \qquad \text{Eqn.6}$$

Figure 9 below compares Equation 6 to the Tjavaras model and the NLTD FEA results. This equation is discussed later in Section 9.

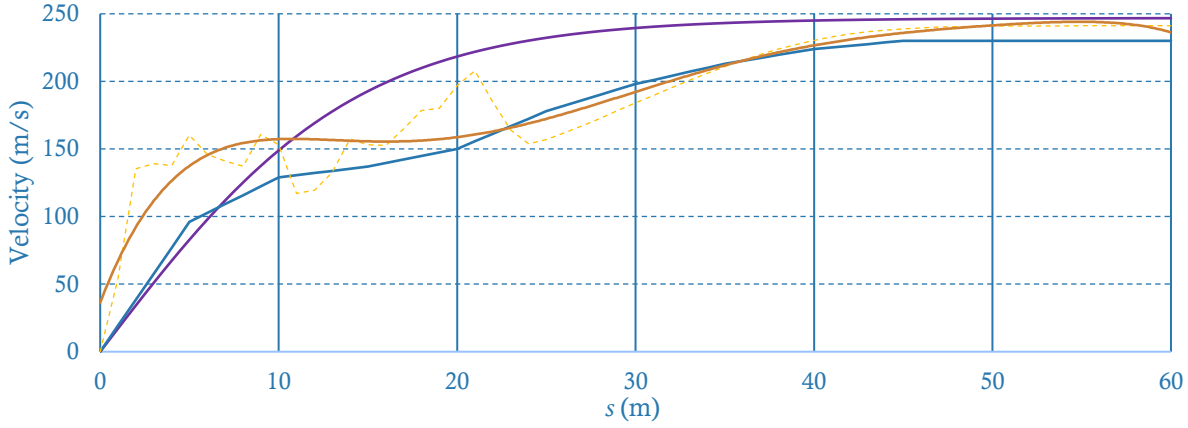

Figure 9: Equation 6 (purple) shown against Figure 8.

5. IMPROVEMENTS TO THE ANALYTICAL MODEL

Whilst accurate to the data given in Table 1, the previous model can still be refined to better represent snapback. These refinements include calculating the cross-sectional properties of the rope, defining segment length based on buckling, and modelling external interactions. Breaking time, effective celerity, and mass scaling may also be considered but, for brevity, are not discussed here.

5.1. Accurate Sectional Properties of Mooring Lines

As noted above, the analysis thus far has considered a homogeneous circular cross-section, however, the actual cross sections of mooring lines are anything but, as shown below in Figure 10.

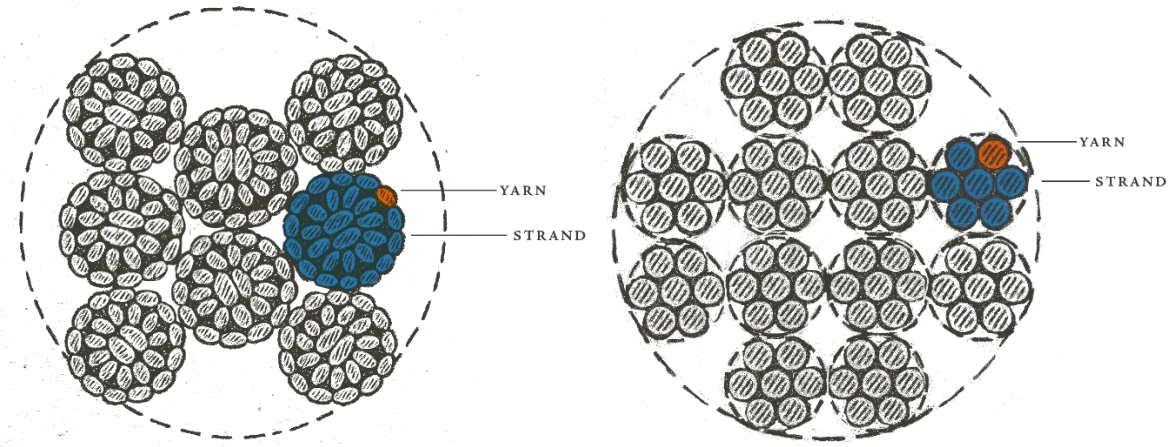

Figure 10: Cross section of a mooring line. 8-strand (left), 12-strand (right).

By calculating the cross-sectional area and second moment of area of these geometries, as shown in Table 3, it can be observed that the axial and flexural stiffnesses of a mooring line are much lower. This in turn means that the magnitude of dynamic buckling increases as the flexural stiffness decreases, and that the velocity in the system increases as the mass decreases for a given density.

Table 3: Parameters for Computational Model of Snapback

Parameter	8-Strand	12-strand
Strand Radius	$\frac{D}{2\sqrt{7}+2}$	$\frac{D}{2\sqrt{10}+2}$
Effective Area	$0.602\ A$	$0.693\ A$
Effective Second Moment of Area	$0.453\ I$	$0.626\ I$
Effective Polar Second Moment of Area	$0.453\ I_P$	$0.626\ I_P$

5.2. Segment Length Based on Buckling

For any transient analysis, for the purposes of ensuring force waves cannot pass over elements entirely between timesteps, the maximum timestep length is given by:

$$t_{max} = \frac{l_{min}}{c} \qquad \text{Eqn.7}$$

Where l_{min} represents the length of the smallest segment. This length can be calculated using Euler-buckling such that each individual segment is at or close to the squash length for the section:

$$P_{cr} = \sigma_{cr} A = \frac{\pi^2 EI}{L^2}$$

$$L_{squash} = \sqrt{\frac{\pi^2 EI}{\sigma_{cr} A}} \qquad \text{Eqn.8}$$

Because Equation 8 can be expressed algebraically in terms of the diameter of the mooring line, it

follows that the squash length can be given in terms of the diameter of the line. For illustrative purposes, the 8-strand case is calculated:

$$L_{squash} = \sqrt{\frac{\pi^2 EI}{\sigma_{cr} A}} = C_L \cdot D = \sqrt{\frac{0.453\pi^2 E \cdot A \cdot D^2}{16\sigma_{cr} A}} \qquad \text{Eqn.9}$$

Though the squash length changes as a function of the material and cross section, by Equation 9 it is typically observed that $C_L = 2-3$. A reduction in the number of segments by way of $l_{min} \cong C_L \cdot D$ produces a linear improvement in computational time.

5.3. External Interactions

During snapback, mooring lines interact with the rigid elements around them, such as vessels or wharves. This can be modelled by adding members to the matrix with piecewise stiffness whereby E=0 GPa, except when the member length is sufficiently short to register 'contact' with a target node. This extension to the model allows for the modelling of ricochet effects and the inclusion of points of redirection of the line, such as a fairlead. Noting that wear can occur either side of the point of contact, the fairlead contact allows for the introduction of curvature to the mooring line and for failure points to be defined either side. Considering Figure 11 below where points A, B, C define the winch, centroid of the front of the fairlead, and the bollard respectively. Points D, E, F exist such that the geometry of the model can be modified to curve about the fairlead radius r_{fl}.

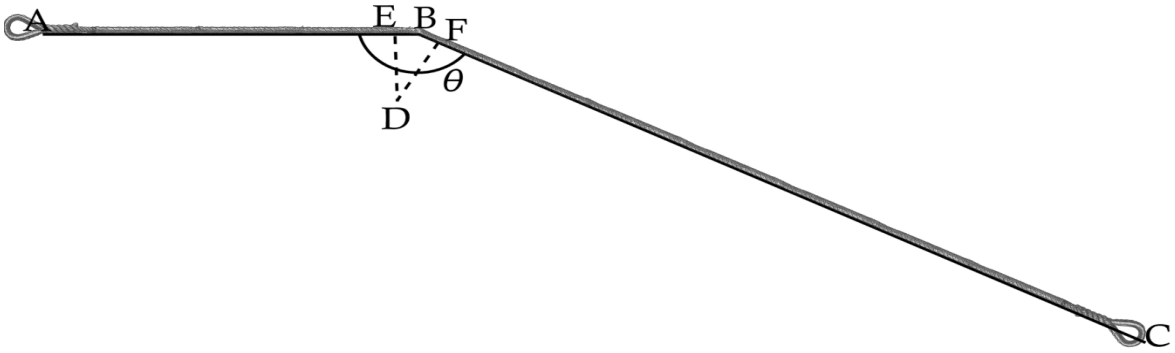

Figure 11: Visualisation of idealised points for defining fairlead contact.

It follows that:

$$\overline{EB} = \overline{BF} = r_{fl} \tan\left(\frac{\pi - \theta}{2}\right) \qquad \text{Eqn.10}$$

From Equation 10, E and F can be defined and an arc of radius r_{fl} subtended between them with segments $l = l_{min}$, each with a piecewise element attached to D. This accurately models contact with the point of redirection, which will be shown to be consequential in Section 6.2.

5.4. Meshing Algorithm

In many cases it is desirable to encode the maximum extents of a snapback path, however, the datasets can be quite large. To manage this, a meshing algorithm is proposed. For M points, the dataset is defined as:

$$P = \{p_i \epsilon \mathbb{R}^3\}_{i=1}^{M} \qquad \text{Eqn.11}$$

The geometric centre of P is given by:

$$p_c = \frac{1}{M} \sum_{i=1}^{M} p_i \epsilon \mathbb{R}^3 \qquad \text{Eqn.12}$$

A cube $\boldsymbol{C}$, with edge length Lc and centre p_c is expressed using the uniform norm:

$$\boldsymbol{C} = \left\{ v \epsilon \mathbb{R}^3 : \|v - p_i\|_\infty \leq \frac{L}{2} \right\} \qquad \text{Eqn.13}$$

$$Lc = \sqrt{(x_{max} - x_{min})^2 + (y_{max} - y_{min})^2 + (z_{max} - z_{min})^2} \qquad \text{Eqn.14}$$

$$x_{max}, x_{min}, y_{max}, y_{min}, z_{max}, z_{min} \epsilon\ P$$

A target number of vertices for the mesh $V(n)$ is then selected by:

$$V(n) = 6n^2 - 12n + 8, \qquad n \epsilon \mathbb{N} \qquad \text{Eqn.15}$$

Where n describes the number of vertices on an edge of the cube. The cartesian coordinates of each vertex can assigned to the six faces of $\boldsymbol{C}$ with equidistant $\mathbb{R}^2$ lattices. This produces a cube mesh of the desired resolution that encapsulates the snapback path dataset, as shown in Figure 12.

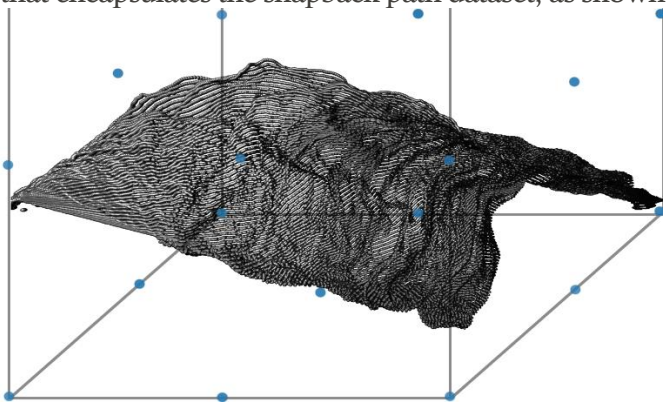

Figure 12: A cube of n=3 encapsulating a snapback path analysis dataset.

$V(n)$ spheres are described with centroids at each vertex. The spheres are expanded by some variable radius within a loop and checked at each step to see if they contain any points from P. When a sphere contacts a point in P, that point is the closest point to the vertex and a unique vector mapping is created. Once all vectors are described, the cube can be topologically transformed to create a volume that contains the dataset. The reduction in data is typically between 99.7 – 99.99% depending on n. An output from the algorithm is shown below in Figure 13.

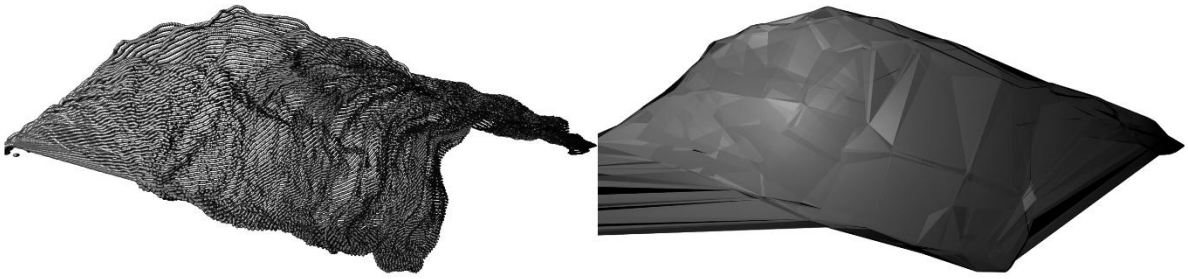

Figure 13: A dataset for a snapback path (left), the mesh for the path (right).

6. VALIDATION AGAINST PHYSICAL TESTING

To demonstrate the suitability of the computational method incorporating the modifications proposed in Section 5, existing physical testing with publicly available information was reproduced. The test configuration adopted for the BMA Hay Point Australia testing (3, 4) was modelled and the output path and velocities were compared to the publicly available results.

6.1. Snapback Velocity

Hodgins et al. note that the peak velocity observed in the physical testing occurred just behind the installed barrier at approximately 400 m/s for an 85t synthetic line parted at 60% Line Design Breaking Force (LDBF). Figure 14 shows the model alongside the physical testing, whilst Figure 15 shows them overlaid. Figure 16 shows their velocities, for which the model was 96.4% accurate.

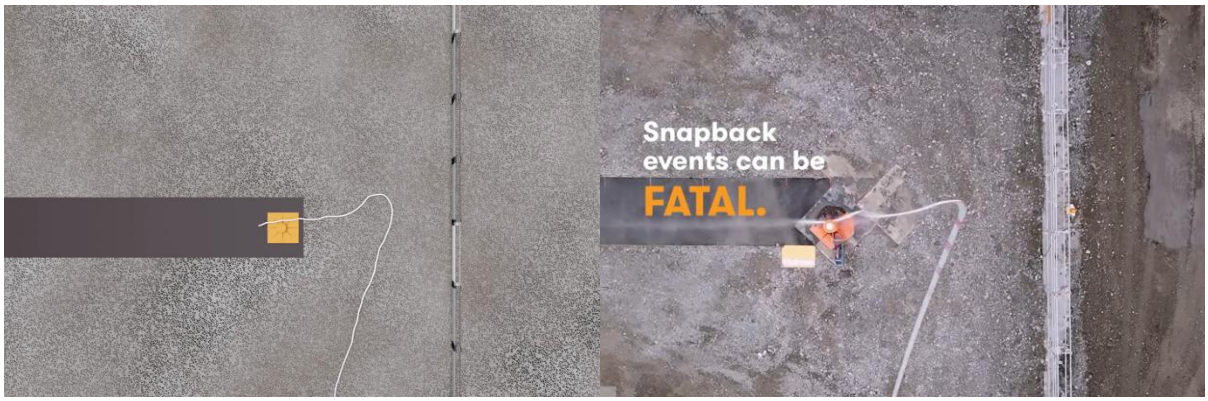

Figure 14: Computational snapback model (left), BMA physical testing (right).

Figure 15: Computational snapback model over BMA physical testing. Images are sourced from Holmes Solutions YouTube (17) and reproduced with permission.

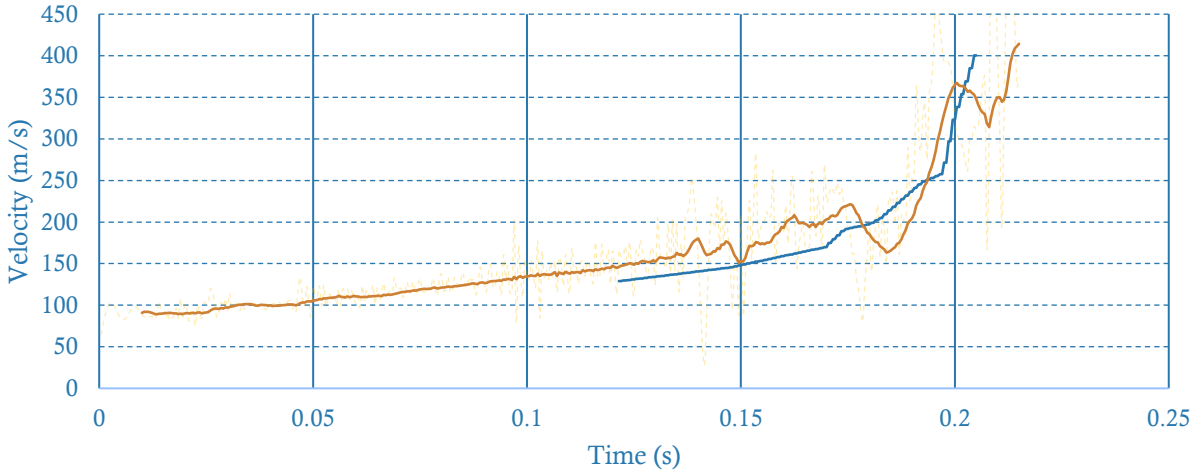

Figure 16: Computational snapback model of BMA Hay Point test: orange, Empirical test data: blue.

6.2. Snapback Path

In addition to velocity, the spatial limits of the test were compared. Interactions with the redirection bollard were modelled using the techniques proposed in Section 5.3, and both spatial and velocity data was used to produce heatmaps of velocity. Figure 17 shows the mooring line interaction with the redirection bollard, whilst Figure 18 shows the mooring line path and velocity.

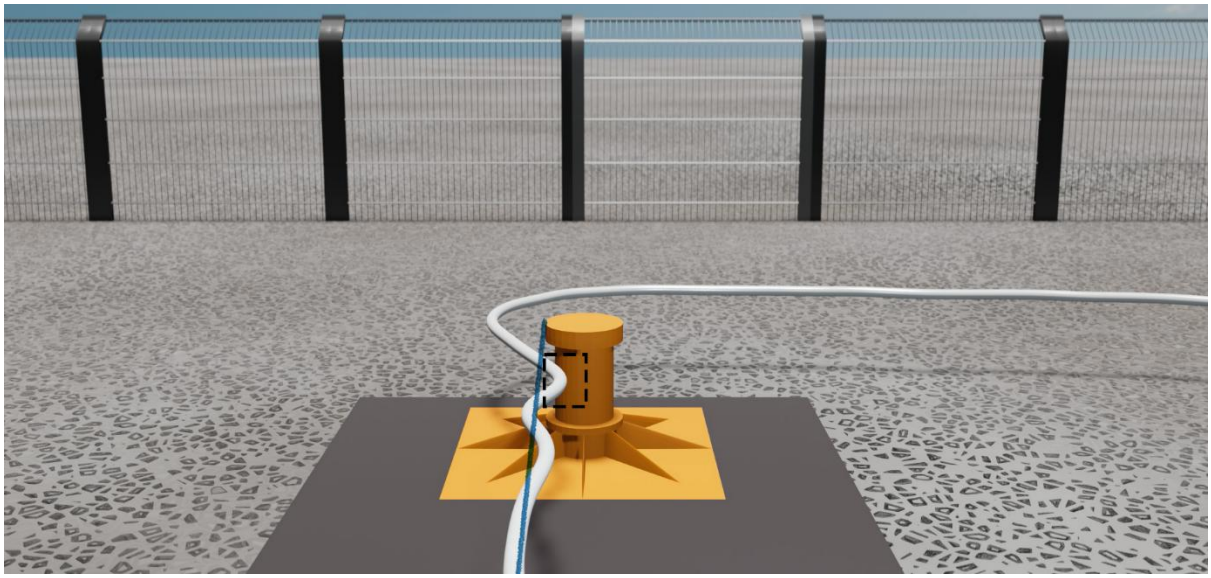

Figure 17: Computational model of BMA test. Dynamic buckling and physical interactions with the bollard change the tangent point and cause the mooring line to move leftward.

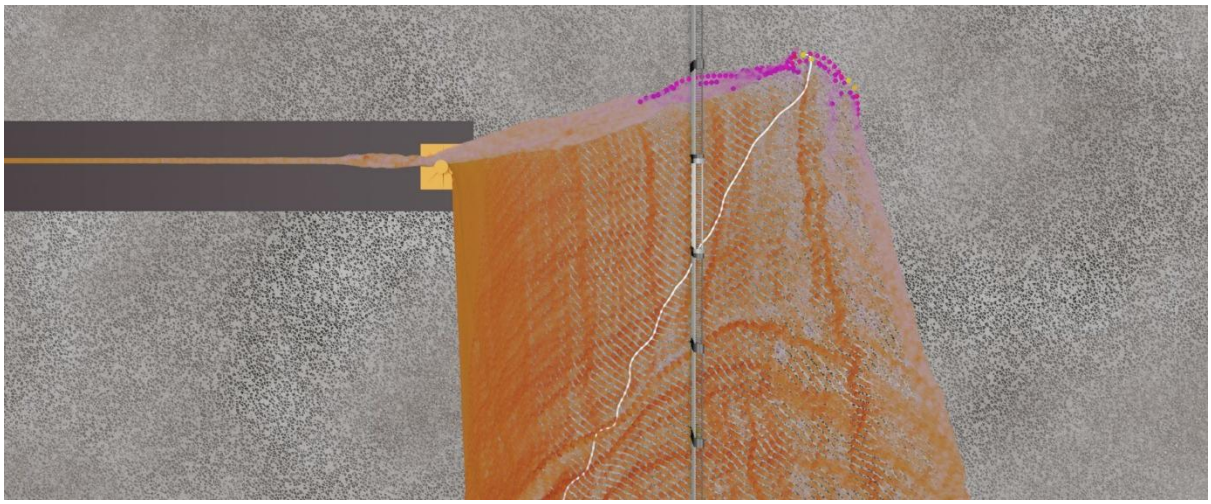

Figure 18: Computational model of the BMA test. Regions in orange are less than 200 m/s. Regions in purple are less than 400 m/s. Bright yellow points are locations where the mooring line velocity exceeded 400 m/s.

6.3. Results of Validation

It was observed that the computational model was 97% accurate in terms of velocity and greater than 99% accurate in terms of path. The modelling of physical interactions and dynamic buckling allowed for the line to interact with the redirection bollard and bias outwards towards its convex side of curvature, which was also observed in the physical testing.

7. COMPUTATIONAL SNAPBACK PATH ANALYSIS

As mentioned in Section 3, historical snapback zones were representative of vessel-side snapback, where the position of mooring infrastructure is invariant. Port-side snapback is more complicated, as many different vessels call port, each with unique mooring arrangements. Further, tides and vessel motion continuously affect line length and geometry. To address this, the computational efficiencies of Sections 4.3 and 5.2 can be adopted to solve large volumes of snapback models. With appropriate use of vessel motions per BS6349 and PIANC guidelines, and statistical analysis of the variability of mooring infrastructure, it is possible to generate large datasets covering all expected vessel classes, mooring arrangements, tides, and motions for a given port.

7.1. Case Study: Example Snapback Path Analysis Dataset

To illustrate this, an anonymised dataset is given from a series of Australian ports. In each case, the vessels were bulk carriers between 180k and 250k DWT and each mooring configuration contained 16 mooring lines. Statistical analysis of the positions of the mooring infrastructure was undertaken and compared to a hindcast of vessels to demonstrate adequate coverage. The vessels assessed are given in Appendix B. The meshing algorithm proposed in Section 5.4 was used and rendered into BIM models for the ports, with an example shown in Figure 19, though the facility is blurred to preserve its anonymity. A summary of total models analysed is given in Table 4.

Table 4: Summary of Case Study Models

Port/Berth	Vessels Modelled	Mooring Configurations	Parting Locations	Total Paths Modelled
1	4	30	2	25,920
2	4	30	2	25,920
3	4	16	2	13,824
4	4	16	2	13,824
5	4	55	3	71,280
6	4	55	3	71,280
7	4	55	3	71,280
8	4	55	3	71,280
Total:				364,608
Estimated Data Points:				6.2×10^{12}

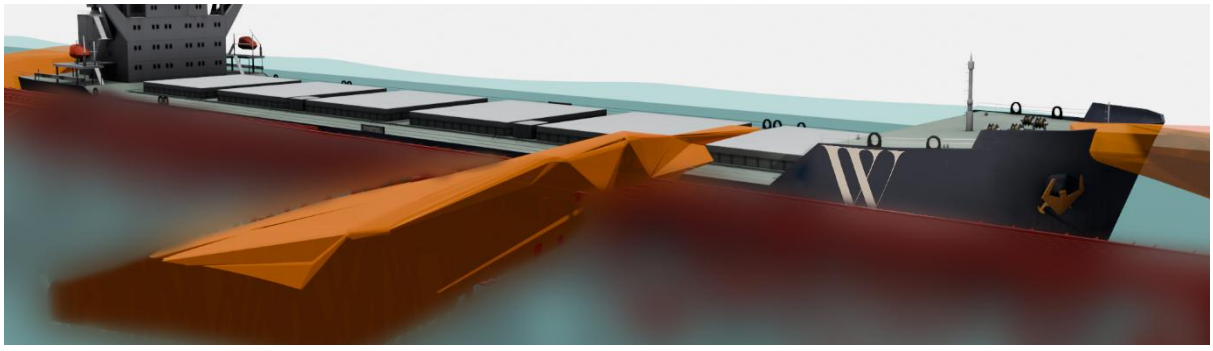

Figure 19: Snapback paths for a ballast bulk carrier at HAT.

7.2. Case Study: Results and Discussion

In almost all cases, snapback paths modelled were larger than those given in Figure 1, supporting their retirement in OCIMF MEG4. It was observed that breast lines, largely as a function of vessel motion with respect to the line length, displayed vastly wider paths than previously estimated, as shown in Figure 20. In some cases, the area of the snapback path was eight times larger than previous estimates.

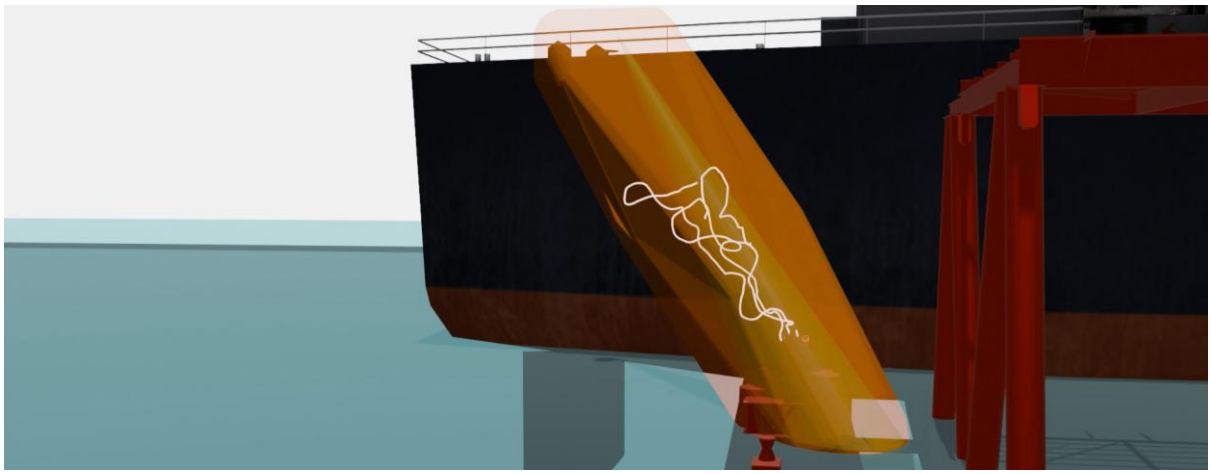

Figure 20: Snapback path of breast lines. the green cone is 10 degrees per MEG1.

It was also shown, in the case of parting at the winch, that for dolphin berths snapback paths could move out horizontally over the facility, rather than down towards the dolphins themselves. This has been observed in cases such as BMA Hay Point. Snapback velocities exceeding 200 m/s were common for tensions greater than 50t, and in most cases achieved average speeds of over 70 m/s, consistent with Table 1. Figure 21 and Table 5 below illustrate this.

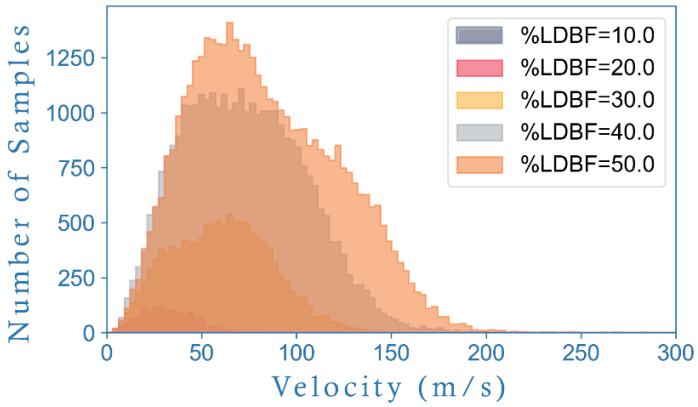

Figure 21: Distribution of snapback velocities for 135t polypropylene line.

Table 5: Velocity percentiles for snapback analyses from Figure 21.

Load (t)	50th Percentile Velocity (m/s)	95th Percentile Velocity (m/s)	99th Percentile Velocity (m/s)	Maximum Velocity (m/s)
26.5	32	59	70	79
39.8	61	105	127	151
53.0	70	127	153	229
66.3	78	151	176	359

8. SNAPBACK ARRESTING STRUCTURES

Snapback arresting structures remain an active area of research for the author. As noted previously, design practices in Australia have adopted quasi-static force deflection analysis for barriers. Theoretical failure modes predicted by some research (2) and empirical test data (3, 4) has shown that high-modal behaviour is expected with localised failures. Using the velocity and path information calculated in this paper, explicit dynamic models were constructed to simulate the impact of a mooring line at 200 m/s into both steel plate and steel grating; both observed in

Australian practice. The results, shown in Figure 22 as one example, show that localised rupture at the site of impact is expected with shrapnel achieving velocities of 100 m/s. Promisingly, in the case of shipping containers used for temporary protection, the inclusion of water tanks within the container arrested the line and the shrapnel within 0.3 m.

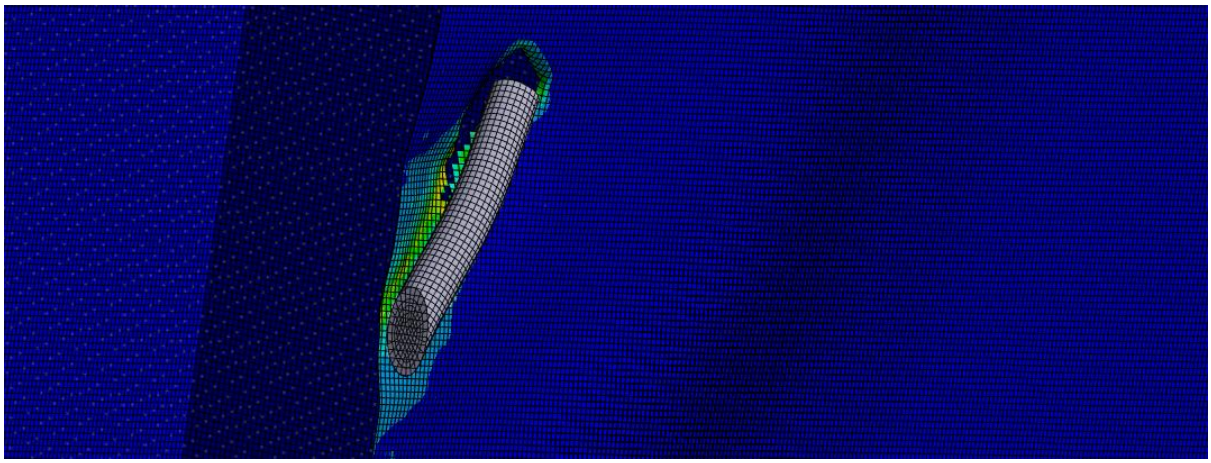

Figure 22: Mooring line impact on a shipping container wall at 200 m/s.

9. FINDINGS AND OBSERVATIONS

9.1. Snapback Velocity Findings

The results of this work show strong agreement with both contemporary and historical physical testing, validating the observation that peak snapback event velocities can exceed 200 m/s. It was observed in the background literature (1) that there was relative invariance between the peak velocities of slow and fast breaking lines, which is contrary to historical observations that showed that energy losses were significant. Whilst computational solutions for energy loss are still being explored, it may be possible to modify Equation 6 with an energy loss factor to give simple approximations for peak velocity to enable ports to quantify their risk without computation.

9.2. Snapback Path Findings

Validating the decision by OCIMF to rescind snapback zones from MEG4, it was observed that snapback paths can be substantially larger than previously estimated, especially for short mooring lines with large tides or vessel motions. However, it is possible to model snapback path and velocity accurately for a given facility provided the range of vessels and mooring configurations is known. Through meshing algorithms, file sizes can be many orders of magnitude less than model data and suitable for use in modern BIM software. Though snapback paths may be larger, future works to integrate snapback path analysis with dynamic mooring analysis may allow for the selection of reduced paths based on the particular lines and tensions modelled. Further, it may be possible for ports to integrate these results into BIM models and update them dynamically for each new vessel, rather than adopting total envelopes for their facilities.

9.3. Arresting Structure Findings

The explicit dynamic analysis undertaken on plate and grating rigid barriers demonstrates high modal wave response behaviour and localised failure producing shrapnel, consistent with physical testing undertaken by others. It may be demonstrated that rigid barriers work for lower velocity impacts, or with different structural configurations, but this is the topic of ongoing research. In the interim, high-tensile cable barriers and water filled containers have both been shown to adequately arrest high velocity snapback events.

10. CONCLUDING REMARKS

Whilst these works have demonstrated the terrifying potential of mooring line snapback, they have also demonstrated that such events can be quantified, modelled, and even arrested. Closed form equations for snapback velocity have been demonstrated that give approximations of detailed computational analysis, allowing ports to make reasonable estimates for potential snapback velocity at their facilities. The author, with the support of Ports Australia and others, is currently pursuing full-scale testing in Australia in 2026 to better quantify the response of arresting structures and the energy losses that occur during the parting of lines. With this information available, it is anticipated that the remaining questions posed by this work can be answered, and through the report of PIANC WG 251, ports worldwide will be able to quantify snapback risk at their facilities, mitigate it, and save lives.

11.REFERENCES

1. A. A. Tjavaras. The Mechanics of Highly Extensible Cables. Journal of Sound and Vibration. 1998;213:709-37.
2. Arnold C.Y. Yong NTKL, Scott J. Menegon. Collision Actions on Structures. Boca Raton: CRC Press; 2022 14/09/2022.
3. K Hodgins RK, B. Poulter, Validating Snapback Risk. Coasts and Ports Australia; 15/08/2023; Sunshine Coast, Queensland: Engineers Australia; 2023.
4. Keane R. Snapback Characterisation for Arresting Structure Design: Physical Testing Insights. PIANC APAC Conference 2024 – Sydney; Sydney, Australia: PIANC; 2024.
5. Australian Maritime Safety Authority. Maritime Safety Awareness Bulletin - Issue 2: Thinking - Mooring Safety. Canberra; 2015 September 2015.
6. Oil Companies International Marine Forum. Mooring Equipment Guidelines 4th Edition. Livingston, Scotland; 2018.
7. UK P&I Club. Understanding Mooring Incidents In: UK P&I Club, editor. LP News. London: Thomas Miller P&I Ltd; 2009.
8. Butler J, editor Snapback to the Future: Mooring Line Safety for All. PIANC Annual General Assembly; 2025; Busan, South Korea: PIANC.
9. Parker JEWaEL. Recoil Properties of Rope. Washington: U.S. Coast Guard; 1966 18/11/1966.
10. Feyrer K. Break Tests Carried Out on Various Ropes in Order to Determine the energy of Lash-Back at Break. Stuttgart: University of Stuttgart; 1978.
11. Bitting KR. A Snapback Evaluation Technique for Synthetic Lines. Washington: United States Coast Guard; 1982 May 1982. Contract No.: USCG-D-29-82.
12. Prentice G. Synthetic Line Snapback. 23rd Annual Technical Symposium. Washington: Association of Scientists and Engineers of the Naval Sea Systems Command; 1986.
13. OCIMF. The Hazards of Snap-back: Initial learnings from a serious incident of mooring line failure. London: OCIMF; 2015.
14. Marine Accident Investigation Branch. Report on the investigation of the failure of a mooring line on board the LNG carrier Zarga while alongside the South Hook Liquefied Natural Gas terminal, Milford Haven resulting in serious injury to an ofcer on 2 March 2015. London: Marine Accident Investigation Branch,; 2017 June 2017.
15. OCIMF. Mooring Equipment Guidelines 1st Edition. London: Witherby & Co. Ltd.; 1992.
16. Clark IC. Mooring and Anchoring Ships Volume 1: Principles and Practice. Institute TN, editor. England: Newnorth Print Ltd and The Nautical Institute; 2009.
17. Solutions H. Dangers of Mooring Line Snapback Youtube: Youtube; 2022 [Available from: https://www.youtube.com/watch?v=AHMdYf7XL14.

APPENDIX A – GENERAL FORMS OF M AND P

The Matrix **M** is a 13 x 13 matrix modified from that originally proposed by Tjavaras et al. and with nomenclature as defined by (1).

$$\mathbf{M} = [\mathbf{M}_1\ \mathbf{M}_2\ \mathbf{M}_3\ \mathbf{M}_4\ \mathbf{M}_5\ \mathbf{0}]$$

Where:

$$\mathbf{M}_1 = \begin{bmatrix} 0 & 0 & 0 & \frac{-m}{f'(\varepsilon)} & 0 & 0 \\ 0 & 0 & 0 & 0 & -(m+m_a) & 0 \\ 0 & 0 & 0 & 0 & 0 & -(m+m_a) \\ -1 & 0 & 0 & 0 & 0 & 0 \\ 0 & 0 & 0 & 0 & 0 & 0 \\ \cdots & \cdots & \cdots & \cdots & \cdots & \cdots \\ 0 & 0 & 0 & 0 & 0 & 0 \end{bmatrix}$$

$$\mathbf{M}_2 = \begin{bmatrix} \frac{-2m(v\beta_3 - w\beta_2)}{f'(\varepsilon)} \\ -2\left[\left(\rho_{medium}\frac{\pi d^2}{4} + m_a\right)(\beta_3 U_c - \beta_0 V_c - \beta_1 W_c) + m(w\beta_1 - u\beta_3)\right] \\ 2\left[\left(\rho_{medium}\frac{\pi d^2}{4} + m_a\right)(\beta_2 U_c - \beta_1 V_c + \beta_0 W_c) + m(v\beta_1 - u\beta_2)\right] \\ 0 \\ 2(1+\varepsilon)\beta_3 \\ -2(1+\varepsilon)\beta_2 \\ 0 \\ \cdots \\ 0 \end{bmatrix}$$

$$\mathbf{M}_3 = \begin{bmatrix} \frac{-2m(w\beta_3 + v\beta_2)}{f'(\varepsilon)} \\ 2\left[\left(\rho_{medium}\frac{\pi d^2}{4} + m_a\right)(\beta_2 U_c - \beta_1 V_c + \beta_0 W_c) - m(u\beta_2 - w\beta_0)\right] \\ 2\left[\left(\rho_{medium}\frac{\pi d^2}{4} + m_a\right)(\beta_3 U_c - \beta_0 V_c - \beta_1 W_c) + m(v\beta_0 - u\beta_3)\right] \\ 0 \\ -2(1+\varepsilon)\beta_2 \\ -2(1+\varepsilon)\beta_3 \\ 0 \\ \cdots \\ 0 \end{bmatrix}$$

$$\mathbf{M}_4 = \begin{bmatrix} \frac{-2m(w\beta_0 + v\beta_1)}{f'(\varepsilon)} \\ 2\left[\left(\rho_{medium}\frac{\pi d^2}{4} + m_a\right)(\beta_1 U_c + \beta_2 V_c + \beta_3 W_c) - m(u\beta_1 + w\beta_3)\right] \\ 2\left[\left(\rho_{medium}\frac{\pi d^2}{4} + m_a\right)(\beta_0 U_c + \beta_3 V_c - \beta_2 W_c) + m(u\beta_0 - v\beta_3)\right] \\ 0 \\ 2(1+\varepsilon)\beta_1 \\ 2(1+\varepsilon)\beta_0 \\ 0 \\ \cdots \\ 0 \end{bmatrix}$$

$$\mathbf{M}_5 = \begin{bmatrix} \dfrac{-2m(w\beta_1 - v\beta_0)}{f'(\varepsilon)} \\ -2\left[\left(\rho_{medium}\dfrac{\pi d^2}{4} + m_a\right)(\beta_0 U_c + \beta_3 V_c - \beta_2 W_c) - m(u\beta_0 + w\beta_2)\right] \\ 2\left[\left(\rho_{medium}\dfrac{\pi d^2}{4} + m_a\right)(\beta_1 U_c + \beta_2 V_c + \beta_3 W_c) + m(v\beta_2 + u\beta_1)\right] \\ 0 \\ -2(1+\varepsilon)\beta_0 \\ 2(1+\varepsilon)\beta_1 \\ 0 \\ \dots \\ 0 \end{bmatrix}$$

The Vector **P** is defined as:

$$\mathbf{P} = \begin{bmatrix} \dfrac{S_b\Omega_2}{f'(\varepsilon)} - \dfrac{S_n\Omega_3}{f'(\varepsilon)} - \dfrac{w_0}{f'(\varepsilon)}(\beta_0^2 + \beta_1^2 - \beta_2^2 - \beta_3^2) - {}^1\!/_2\,\rho_{medium} d\pi C_{dt}(t_{n-1})\dfrac{(u-u_c)|u-u_c|}{f'(\varepsilon)}\sqrt{1+\varepsilon} \\ f(\varepsilon)\Omega_3 - S_b\Omega_1 - 2w_0(\beta_1\beta_2 - \beta_0\beta_3) - {}^1\!/_2\,\rho_{medium} d\pi C_{dp}(t_{n-1})(v-v_c)\sqrt{(v-v_c)^2 + (w-w_c)^2}\sqrt{1+\varepsilon} \\ S_n\Omega_1 - f(\varepsilon)\Omega_2 - 2w_0(\beta_1\beta_3 + \beta_0\beta_2) - {}^1\!/_2\,\rho_{medium} d\pi C_{dp}(t_{n-1})(w-w_c)\sqrt{(v-v_c)^2 + (w-w_c)^2}\sqrt{1+\varepsilon} \\ \Omega_2 w - \Omega_3 v \\ \Omega_3 u - \Omega_1 w \\ \Omega_1 v - \Omega_2 u \\ {}^1\!/_2\,(\beta_1\Omega_1 + \beta_2\Omega_2 + \beta_3\Omega_3) \\ -{}^1\!/_2\,(\beta_0\Omega_1 - \beta_3\Omega_2 + \beta_2\Omega_3) \\ -{}^1\!/_2\,(\beta_3\Omega_1 + \beta_0\Omega_2 - \beta_1\Omega_3) \\ {}^1\!/_2\,(\beta_2\Omega_1 + \beta_1\Omega_2 - \beta_0\Omega_3) \\ 0 \\ \left(\dfrac{GI_p}{EI} - 1\right)\Omega_1\Omega_3 - \dfrac{1}{0.45EI}S_b(1+\varepsilon)^3 \\ \left(1 - \dfrac{GI_p}{EI}\right)\Omega_1\Omega_2 + \dfrac{1}{0.45EI}S_n(1+\varepsilon)^3 \end{bmatrix}$$

APPENDIX B – CASE STUDY VESSEL ARRANGEMENTS

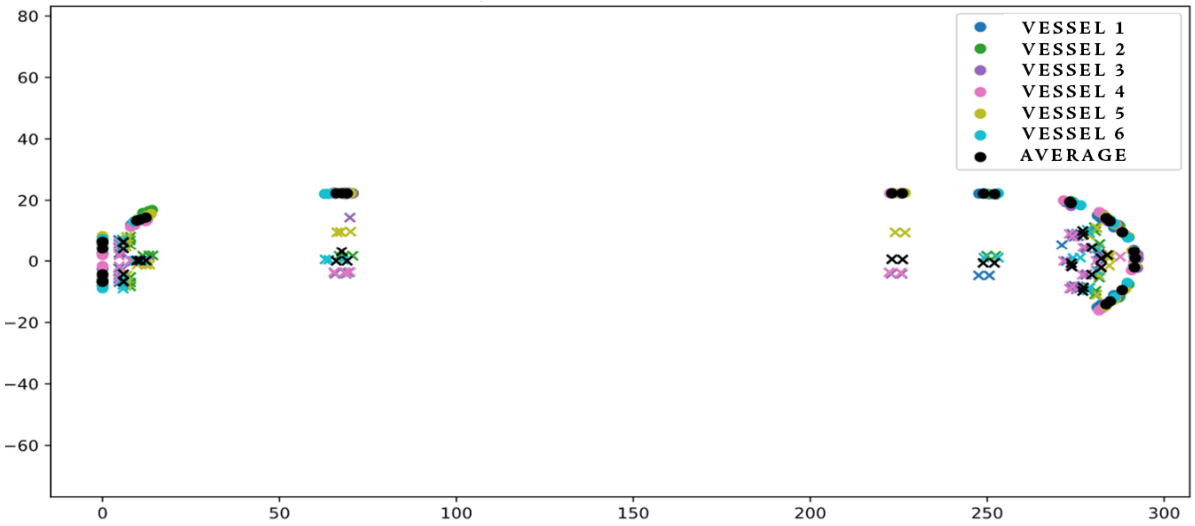

Figure 23: 180k DWT Bulk Carriers.

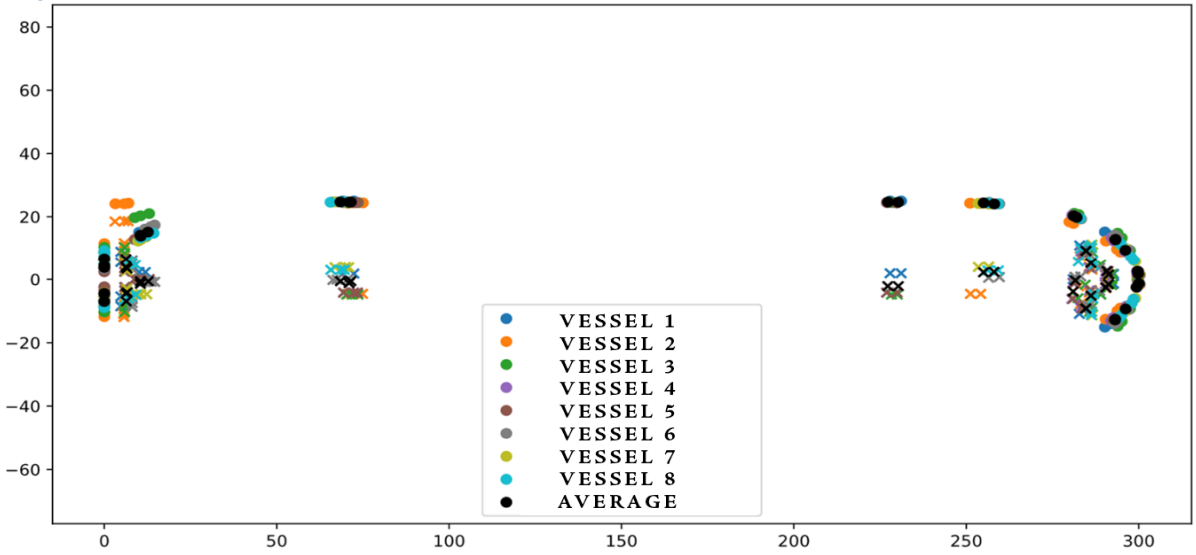

Figure 24: 210k DWT Bulk Carriers.

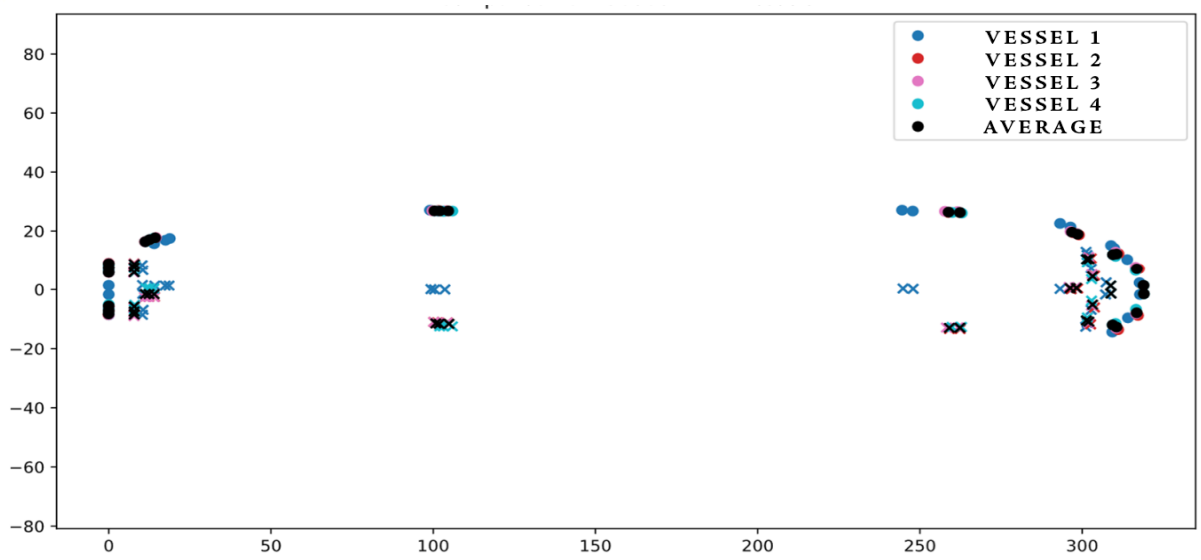

Figure 25: 230k DWT Bulk Carriers.

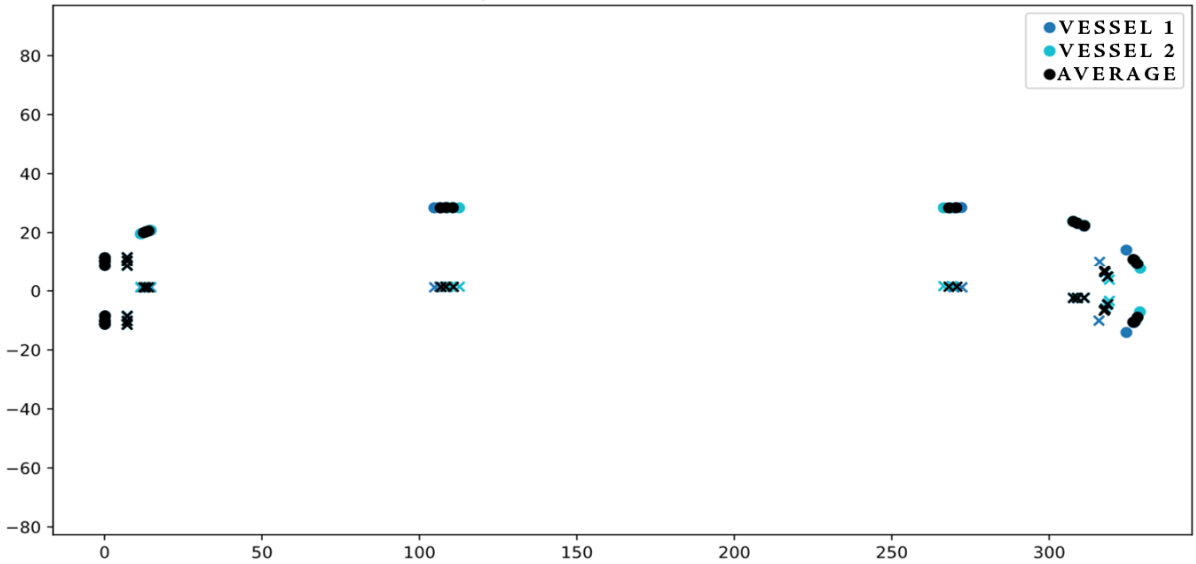

Figure 26: 250k DWT Bulk Carriers.